JOURNAL OF GEOPHYSICAL RESEARCH, VOL. 112, B08310, doi:10.1029/2006JB004712, 2007

P and *S* velocity structure of the crust and the upper mantle beneath central Java from local tomography inversion

I. Koulakov,[1,2] M. Bohm,[1] G. Asch,[1] B.-G. Lühr,[1] A. Manzanares,[1] K. S. Brotopuspito,[3] Pak Fauzi,[4] M. A. Purbawinata,[5] N. T. Puspito,[6] A. Ratdomopurbo,[7] H. Kopp,[8] W. Rabbel,[9] and E. Shevkunova[10]

Received 23 August 2006; revised 3 May 2007; accepted 5 June 2007; published 21 August 2007.

[1] Here we present the results of local source tomographic inversion beneath central Java. The data set was collected by a temporary seismic network. More than 100 stations were operated for almost half a year. About 13,000 *P* and *S* arrival times from 292 events were used to obtain three-dimensional (3-D) *Vp*, *Vs*, and *Vp*/*Vs* models of the crust and the mantle wedge beneath central Java. Source location and determination of the 3-D velocity models were performed simultaneously based on a new iterative tomographic algorithm, LOTOS-06. Final event locations clearly image the shape of the subduction zone beneath central Java. The dipping angle of the slab increases gradually from almost horizontal to about 70°. A double seismic zone is observed in the slab between 80 and 150 km depth. The most striking feature of the resulting *P* and *S* models is a pronounced low-velocity anomaly in the crust, just north of the volcanic arc (Merapi-Lawu anomaly (MLA)). An algorithm for estimation of the amplitude value, which is presented in the paper, shows that the difference between the fore arc and MLA velocities at a depth of 10 km reaches 30% and 36% in *P* and *S* models, respectively. The value of the *Vp*/*Vs* ratio inside the MLA is more than 1.9. This shows a probable high content of fluids and partial melts within the crust. In the upper mantle we observe an inclined low-velocity anomaly which links the cluster of seismicity at 100 km depth with MLA. This anomaly might reflect ascending paths of fluids released from the slab. The reliability of all these patterns was tested thoroughly.

Citation: Koulakov, I., et al. (2007), *P* and *S* velocity structure of the crust and the upper mantle beneath central Java from local tomography inversion, *J. Geophys. Res.*, *112*, B08310, doi:10.1029/2006JB004712.

1. Introduction

[2] Most of the damaging seismicity and most of the hazardous volcanoes in the world are related to subduction zones. Central Java belongs to these high-risk places in the world, as was proven by the last destructive earthquake in Yogyakarta, 27 May 2006, and eruption activity of Merapi volcano occurred at the same time. Investigation of the structure and the dynamics of subduction complexes is an important task for understanding the mechanisms of influence of deep processes upon the surface. Seismic tomography based on natural seismicity, which is one of the most powerful tools for retrieving reliable three-dimensional (3-D) structures at great depths, can be of great use in obtaining this information [e.g., *Graeber and Asch*, 1999; *Haberland and Rietbrock*, 2001; *Schurr et al.*, 2003; *Koulakov et al.*, 2006].

[3] The area of investigation for this study (Figure 1) covers central Java, Indonesia. It is a small part of a 5000 km long subduction zone called Sunda Arc. Along this Island Arc, which outlines the plate boundaries of Eurasian and Indian-Australian tectonic plates, around 98 active volcanoes are located [*Simkin and Siebert*, 1994]. In the area of central Java, the subduction of the Australian plate under the Sunda block occurs at a rate of about 6.5 cm/yrs [*DeMets et al.*, 1990]. The age of the subducted plate in the central Java area is about 80–100 Ma [*Müller et al.*, 1997], the maximum value in the Indian Ocean. Distribution of seismicity from the worldwide catalogue [*International Seismological Centre* (*ISC*), 2001] shows that

[1]GeoForschungsZentrum Potsdam, Telegrafenberg, Potsdam, Germany.
[2]Now at Trofimuk Institute of Petroleum Geology and Geophysics, Siberian Branch of Russian Academy of Sciences, Novosibirsk, Russia.
[3]Gadjah Mada University, Yogyakarta, Indonesia.
[4]Meteorological and Geophysical Agency, Jakarta, Indonesia.
[5]Directorate of Volcanology and Geological Hazard Mitigation, Bandung, Indonesia.
[6]Institut Teknologi Bandung, Bandung, Indonesia.
[7]Volcanological Technology Research Center, Yogyakarta, Indonesia.
[8]Leibniz Institute of Marine Sciences, Universität Kiel, Kiel, Germany.
[9]Institute of Geosciences, Christian-Albrechts-Universität zu Kiel, Kiel, Germany.
[10]Geophysical Survey, Siberian Branch of Russian Academy of Sciences, Novosibirsk, Russia.

0148-0227/07/2006JB004712$09.00

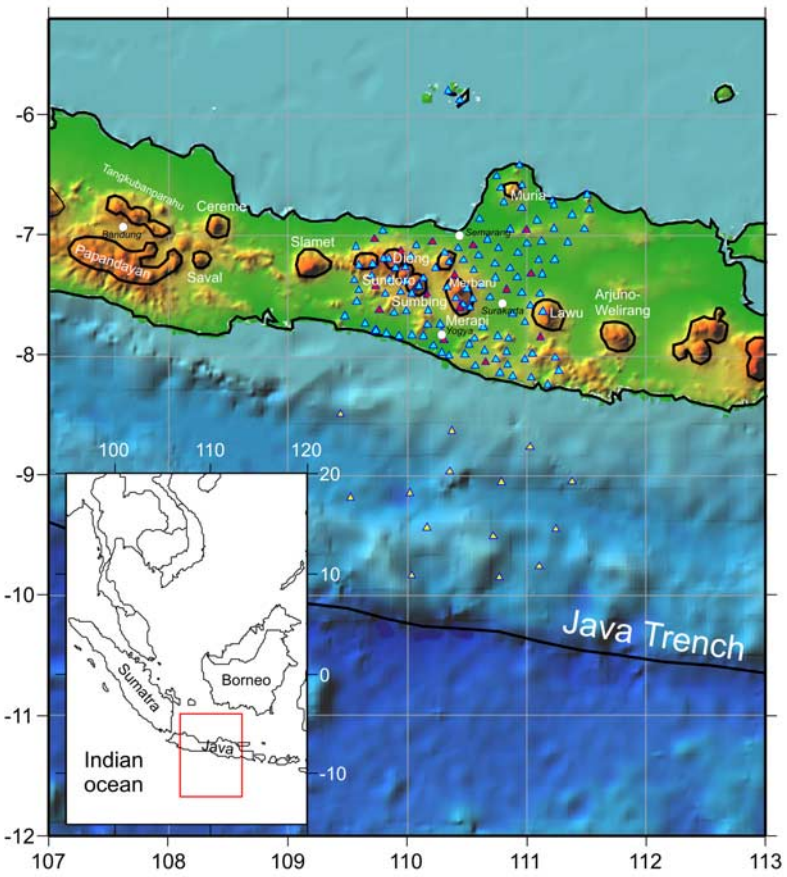

Figure 1. Relief and bathymetry of the study area. The main volcanic complexes are highlighted with black contour lines. The main cities are marked with white circles. Triangles show position of the MERAMEX stations (red, broadband stations; blue, short-period stations; yellow, ocean bottom stations).

the dipping angle of the slab increases gradually from almost horizontal, beneath the offshore part, to very steep (70°–80°), north of Java. Some moderate seismicity at the depth of around 600 km is observed at 6°S longitude beneath the Karimunjawa island group in the Java Sea.

[4] It is clear that subduction plays an important role in producing the volcanic complexes. This connection is observed in almost all existing subduction zones on Earth. However, only in a few areas, such as Japan [*Nakajima et al.*, 2001] or Central Andes [*Graeber and Asch*, 1999; *Haberland and Rietbrock*, 2001; *Schurr et al.*, 2003; *Koulakov et al.*, 2006] the detailed geophysical observations allow quantitative consideration of the role of subduction in the origin of volcanic complexes. In particular, in the Central Andes, low *P* and *S* seismic velocities zones link seismicity clusters at 100–120 km depth with the main volcanic arc [*Schurr et al.*, 2003; *Koulakov et al.*, 2006]. It is presumed that these zones trace the upward migration of fluids rejected from the slab because of the phase transition. These fluids cause decreasing viscosity, and possibly, partial melting. The partially molten materials penetrated into the crust form magma reservoirs which, in some cases, reach the surface and cause the volcanic eruptions.

[5] Previous geophysical studies in central Java were mostly focused on complex investigation of active volcanoes, which present real danger to the local population. Comprehensive research was made for Merapi, one of the most active volcanoes in Indonesia. On the basis of various observations, the beginning of volcanism at Mt. Merapi is estimated at about 40,000 years ago [e.g., *Camus et al.*, 2000]. The occurrence of VEI 4 (Volcanic Explosivity Index) events in the middle to late Holocene [*Gertisser and Keller*, 1998] are an order of magnitude larger than any recorded historical eruption of Merapi, except for the possible VEI 4 event of 1872 [*Simkin and Siebert*, 1994]. The available radiocarbon data further indicate an almost continuous activity of Merapi during the last 2000 years. It was only interrupted by periods of decreasing activity during 600–700 and 1200–1300 years B.P. [*Gertisser and Keller*, 2003].

[6] For a better understanding of the recent volcanic activity, the geophysical structure of the volcanic edifice was intensively investigated [*Müller and Haak*, 2004; *Müller et al.*, 2002; *Wegler and Lühr*, 2001; *Maercklin et al.*, 2000]. Seismological studies carried out by *Ratdomopurbo and Poupinet* [2000] have shown an aseismic zone inside the cone of the volcano. They suggested the idea of two magma reservoirs. A shallow one at 1–2 km depth below the summit may have a high-hazard potential. The deeper one which is considered as the main one is located below 5 km depth [*Ratdomopurbo and Poupinet*, 2000]. This hypothesis was supported by the petrological

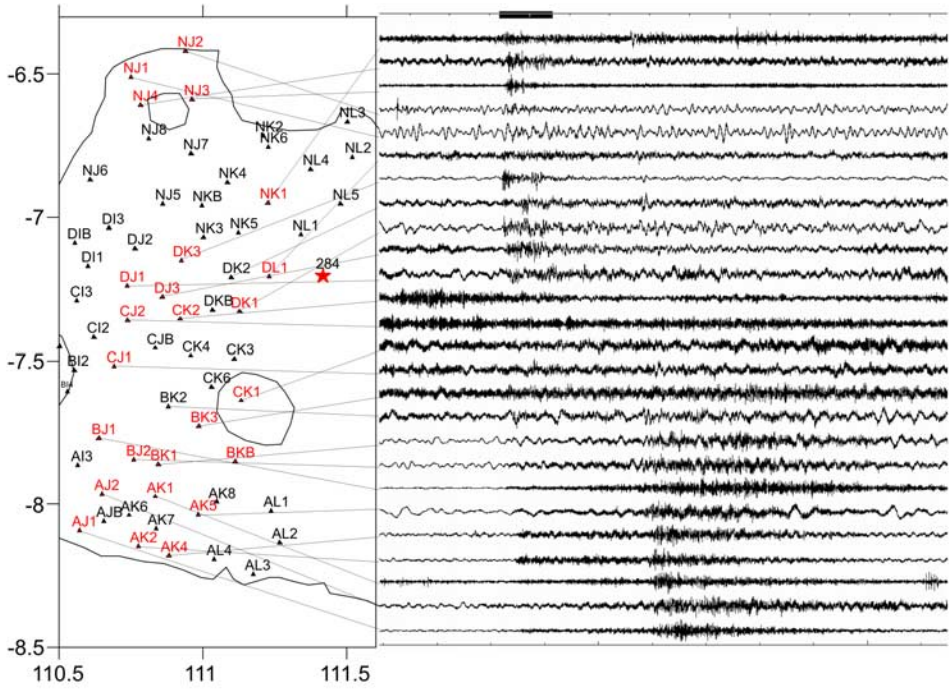

Figure 2. Example of seismic signals from a relatively weak local event recorded by some of the MERAMEX stations. The event is indicated by a red star and is located at a depth of 284 km beneath central Java. The stations whose records are presented are marked with red letters. This image clearly shows a zone of strong attenuation in the center of the study area just behind the volcanic arc.

composition analysis of erupted material [*Purbawinata et al.*, 1997]. On the basis of modeling using GPS and tilt data, *Beauducel and Cornet* [1999] conclude that the feeding magma reservoir can be located between 6 km and 9 km below the summit. High-resolution gravity modeling in [*Tiede et al.*, 2005] also show the evidence of high-density bodies beneath the volcanic summits of Merapi, Merbabu and Telemoyo, that can be interpreted as magma reservoirs.

[7] On the other hand, there are some observations which do not support the hypothesis of magma reservoirs beneath the Java volcanoes. In particular, seismic data from [*Wassermann et al.*, 1998] and the analysis of the deformation data of [*Westerhaus et al.*, 1998] do not support the idea of a shallow magma reservoir. Results of MT measurement and a profile crossing central Java have shown no significant conductivity anomalies for depth below 3 km [*Hoffmann-Rothe et al.*, 2001], but overall low apparent resistivities. According to these data, the maximum of conductivity in the uppermost 3km is observed not beneath the Merapi, but to the north of the main volcanic arc.

[8] Geophysical structure information about the deeper parts beneath Merapi and central Java was quite poor. *Gossler* [2000] analyzed teleseismic events recorded at the broadband stations of the MERAPI monitoring network with the Receiver Function method. However, geometrical effects of the cone 3-D shape prevented obtaining any significant result about the deep structure. Global and regional tomographic models [e.g., *Gorbatov and Kennett*, 2003; *Bijwaard et al.*, 1998] give a quite robust image of the slab starting from the depth of 150–200 km. However, in the upper part, the resolution does not allow getting any reliable feature.

[9] This study is oriented on closing the gap between global and local studies. In 2004, combined amphibious seismological investigations at 110°E have been performed within the Merapi Amphibious Experiment (MERAMEX) project to study a volcanic system as part of an active continental margin. This experiment, with a large number of recording stations and fairly high-distribution density, was designed to get a detailed and reliable image of processes beneath the volcanic chain in central Java. The main purpose of this study is to provide new quantitative constraints about the interior structures of the mantle wedge and crust beneath central Java and to show the ascent paths of fluids and partially molten materials below the volcanic arc. Another purpose of this study is accurate location of the slab-related seismicity that provides reliable information about the shape of the slab.

2. Data Description

[10] The temporary seismological network was in operation for about 150 days from May to October 2004. It consisted of 134 continuously recording seismic stations covering a region of about 150x200 km, of which 106 were short period seismometers, 14 were broadband Guralps, 8 were ocean bottom hydrophones, and 6 were ocean bottom seismometers (Figure 1). The three-component short-period seismometers (Mark L43D or Guralp CMG40T) were equipped by the Earth data loggers (EDL) recording with a sampling frequency of 100Hz. The broadband stations were operated with Guralp seismometers (CMG3T and CMG3ESP) and recorders (SAM). The internal clock of the data loggers were regularly checked against Universal Time (UTC) using the GPS satellite signal. The average

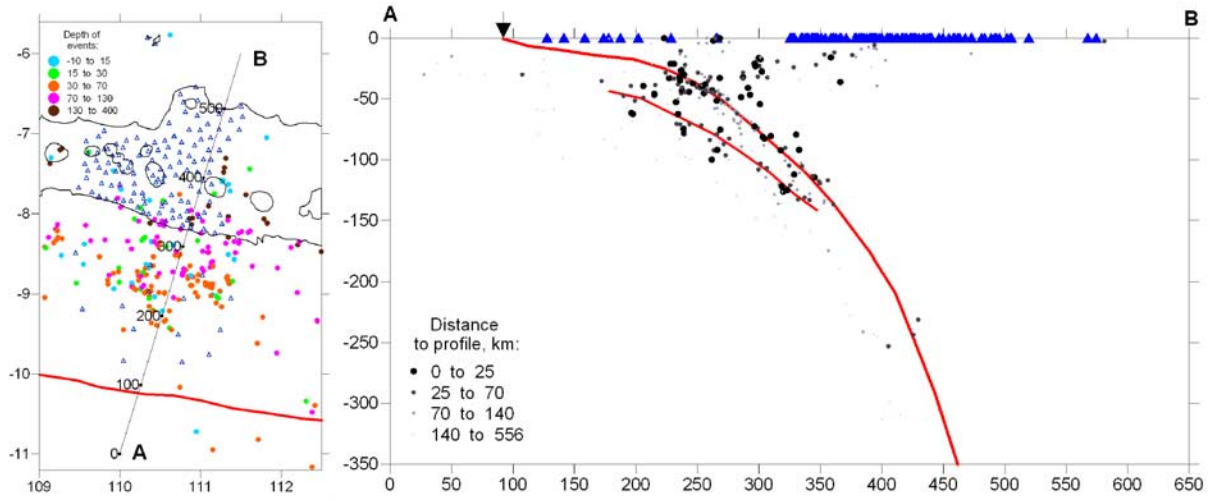

Figure 3. Configuration of the observation system. (left) Map view. Sources used in this study are color coded according to their depth. Open blue triangles are the stations of the MERAMEX network. Red line depicts the position of the trench. (right) Projection of the sources differing in size and intensity depending on distance to the profile, and stations (blue triangles) on the A–B profile, shown in the map view. The location of the trench is marked by an arrow. Supposed positions of the upper limit of the slab and the double seismic zone are highlighted with red lines.

station spacing was about 20 km. Two of the stations were installed 60 km north of the main network on two small islands belonging to the Karimunjawa island group in the Java Sea just above an accumulation of hypocenters at 600 km depth. The ocean bottom hydrophones (OBH) and ocean bottom seismometers (OBS) were deployed offshore on the seafloor and operated for a period of 18 weeks. The station spacing of the ocean bottom instruments was about 40–90 km. During the experiment a total amount of 500 Gbyte of seismological data were acquired.

[11] An example of seismograms from a local event recorded at some stations of the network is presented in Figure 2. In this example the event is relatively weak and located at a depth of about 280 km, that gives us clear difference in recording conditions at different onshore stations. It can be seen that, although the event is beneath the middle of Java, the clearest records are observed at the southern and northern coastal areas. North of Merapi and Lawu volcanoes, the signal seems to be strongly attenuated. Thus the preliminary qualitative consideration of seismograms gives us an idea about the existence of a strong feature beneath central Java. That will be then confirmed by our tomographic results.

[12] In this study we use information from the 292 clearest local events detected during the operation period of the network. In total, 13,800 phases (8000 *P* and 5800 *S* phases) were hand-picked and used for simultaneous location of sources and tomographic inversion. The distributions of the relocated events are shown in horizontal and vertical planes in Figure 3.

3. Algorithm of Local Tomography

3.1. Definition of the Reference Model

[13] Although our algorithm allows utilization of any complicated 3-D velocity model as a reference, in this study we start from a 1-D model. The *P* velocity reference model down to the depth of 20 km was estimated based on results of an active seismic experiment performed in the offshore part of the same study region [*Wagner et al.*, 2007]. For deeper parts we did not have any reliable constrains, therefore, the velocity model below 20 km depth was defined based on the global AK135 model [*Kennett et al.*, 1995]. The resulting model of the initial *P* model is presented in Table 1. For the *S* velocity distribution, we also did not have any a priori information and it was determined according to a fixed *Vp*/*Vs* ratio. We have performed a series of inversions with different *Vp*/*Vs* ratios and found that a value of 1.74 provides minimum RMS values of *P* and *S* residuals (Table 3, section 4.6). It was shown, that although this ratio is important for the source location, it has not significant effect upon the relative velocity variations in the tomographic inversion. The role of this ratio has been investigated in detail and is shown in section 4.6.

[14] In our opinion, definition of a more complicated 1-D reference model from the available data set makes no sense. If very strong perturbations (more than 20% of velocity variations) are expected, the algorithms for estimating an

Table 1. Reference 1-D *P* Velocity Model

Depth, km	*Vp*, km/s
−3	4.3
3	4.9
8	5.7
16	6.9
24	7.1
77	7.8
120	8.05
165	8.17
210	8.3

optimum 1-D model, like VELEST [*Kissling et al.*, 1994], do not provide stable results. In fact, the resulting model obtained in such a way would strongly depend on the ray distribution. Moreover, rays traveling in the crust with rather steep dipping angles (less than 45°) cannot provide reliable constraints for a thin-layered 1-D model.

3.2. Iterative Inversion Algorithm

[15] Here we present a new tomographic algorithm, LOTOS-06 (Local Tomography Software), designed for simultaneous inversion for *P* and *S* velocity structures and source coordinates. This algorithm has already been tested on a number of different data sets with varying study area size, data quality and quantity. It has a quite wide range of possibilities for performing different test and is quite easy to operate. (The LOTOS-06 code can be freely provided to any interested person by I. Koulakov (ivan2art@gmail.com).)

[16] The input data for the tomographic algorithm consist of the absolute arrival times from local seismic events (hours, minutes and seconds) and station coordinates. The iterative inversion algorithm consists of the following steps: (1) Rough positions of sources are determined using a location algorithm based on a 1-D velocity model. (2) The coordinates of the sources are corrected according to another location algorithm which is designed for an arbitrary 3-D model and based on the ray tracing bending method. (3) The parameterization grid for 3-D representation of the velocity anomalies is constructed according to the ray density. (4) The matrix is computed on the basis of raypaths obtained after step 2. (5) The inversion is performed simultaneously for *P* and *S* velocity anomalies, source parameters, and station corrections. (6) The *P* and *S* velocity models are updated and used for the next iteration which consists of the repetition of steps 2, 4, and 5.

[17] Now, let us present a more detailed description of these steps. Step 1, rough location of sources, is based on searching for an absolute extreme of a goal function (GF) which reflects the probability of the source position being at a point in 3-D space. The GF is described in [*Koulakov and Sobolev*, 2006]. For this step, the traveltimes are calculated based on tabulated values computed once for the rays with different epicentral distances and sources depths. In case of the 3-D velocity starting model, the tabulated traveltimes are computed for the 1-D velocity model which is closest to the reference model. The search of the GF extreme is performed starting from the position of the station with minimum arrival time using a coarse grid for rough location and finer grid for final solution. It was shown that this location method is very stable and does not depend on the starting point. In particular, it provides the same resulting source position even if the starting points are located 200 km from each other.

[18] Step 2, location of sources in the 3-D velocity model, is performed on the basis of the rays constructed using the bending method [*Um and Thurber*, 1987]. The source location is based on searching for a maximum gradient of the GF, similarly as in [*Koulakov et al.*, 2006].

[19] Step 3, parameterization, is based on the same approach as used in [*Koulakov et al.*, 2006]. The 3-D velocity anomalies are computed in nodes distributed in the study volume. Velocity distribution between the nodes is interpolated linearly using subdivision of the study volume into tetrahedral blocks. In this study, the nodes are installed in vertical planes which are spaced at 10 km from each other. In each vertical plane, nodes are distributed according to ray density. In areas with small amount of rays the distance between nodes is larger. To avoid an excessive concentration of nodes in areas with high-ray density, we fix the minimum spacing between nodes at 5 km, which is significantly smaller than a characteristic size of the expected anomalies. It is important to note that in our algorithm the resolution of the model does not depend on the grid spacing. It is merely controlled by flattening and regularization parameters during the matrix inversion which is described below. However, since the nodes are placed on planes having a predefined orientation, this can bring some artifacts to the result of the inversion. To reduce the effect of grid orientation we perform the inversion in four differently oriented grids (0°, 45°, 90° and 135°) and stack the results in one model.

[20] Step 4, matrix calculation, is performed along the rays computed by the bending method after the Step 2. The effect of velocity variation at each node on the traveltime of each ray ($\partial t/\partial V$) is computed numerically, as in [*Koulakov et al.*, 2006]. The data vector corresponding to this matrix consists of residuals obtained after the step of source location.

[21] Step 5, inversion, is performed simultaneously for *P* and *S* velocity anomalies, source parameters (4 parameters for each source) and *P* and *S* station corrections. The system of linear equations has the following structure:

$$\left(\frac{\partial t_i}{\partial V_j^P} dV_j^P\right) + 0 + \left(W^{Srce}\frac{\partial t_i}{\partial \sigma_k} d\sigma_k\right) + \left(W^{St\_P} d\tau_{st}^P\right) + 0 = dt_i^P \tag{1a}$$

$$0 + \left(\frac{\partial t_i}{\partial V_j^S} dV_j^S\right) + \left(W^{Srce}\frac{\partial t_i}{\partial \sigma_k} d\sigma_k\right) + 0 + \left(W^{St\_S} d\tau_{st}^S\right) = dt_i^S \tag{1b}$$

$$\left[Sm\_P\ \left(dV_m^P - dV_n^P\right)\right] + 0 + 0 + 0 + 0 = 0 \tag{1c}$$

$$0 + \left[Sm\_S\ \left(dV_m^S - dV_n^S\right)\right] + 0 + 0 + 0 = 0 \tag{1d}$$

$$\left(Re\_P\ dV_j^P\right) + 0 + 0 + 0 + 0 = 0 \tag{1e}$$

$$0 + \left(Re\_S\ dV_j^S\right) + 0 + 0 + 0 = 0 \tag{1f}$$

[22] Here each equation contains five groups corresponding to different unknown parameters. The first and second terms correspond to parameters of *P* and *S* velocity anomalies (dV^P, dV^S). The third term is for corrections of source parameters, σ, which contain source coordinates and origin time. W^{srce} is a weight for controlling the source parameters. The fourth and fifth terms are for determination

Table 2. General Information About the Results Obtained Using Different Inversion and Smoothing Parameters[a]

Model	*Sm_P*	*Sm_S*	*Re_P*	*Re_S*	*Vp/Vs*	Average Deviations of Velocity Anomalies		Variance Reduction	
						P	*S*	*P*	*S*
0.5-1-0-0	0.5	1	0	0	1.983	3.04	3.406	41.21	43.77
0.5-1-1-1	0.5	1	1	1	1.984	2.72	3.64	39.28	43.93
1-2-0-0	1	2	0	0	1.948	2.601	2.829	36.4	40.02
1-2-1-1	1	2	1	1	1.941	2.201	2.873	35.17	39.29
1.5-2.5-1-1[b]	1.5	2.5	1	1	1.924	1.82	2.42	33.67	40.22
2-3-1-1	2	3	1	1	2.01	1.58	2.09	28.26	36.17
3-4-1-1	3	4	1	1	2.04	1.36	1.86	23.64	32.96
3-6-1-1	3	6	1	1	1.96	1.33	1.68	23.41	31.12
4-8-1-1	4	8	1	1	1.96	1.31	1.46	21.62	29.52

[a]*Sm_P* and *Sm_S* are values of *P* and *S* smoothing parameters, respectively; *Re_P* and *Re_S* are *P* and *S* regularization parameters; *Vp/Vs* is the value of Poisson ratio at the check point inside MLA; average amplitude *P* and *S* are average deviations of *P* and *S* velocity anomalies; variance reduction *P* and *S* are the values of variance reduction for *P* and *S* data, respectively, in percent.
[b]Most reliable model.

of *P* and *S* station corrections, $d\tau_{st}^{p}$ and $d\tau_{st}^{p}$. W^{St_P} and W^{St_S} are the weights for the *P* and *S* station corrections. Equations (1a) and (1b) are the main equations with the observed residuals, dt^{P} and dt^{S}, in the right part. The other equations are supplementary ones for controlling smoothness and amplitude of the velocity models. Equations (1c) and (1d) each contain two nonzero elements with opposite signs, corresponding to neighboring parameterization nodes in the model (with indexes *m* and *n*). The data vector corresponding to this block is zero. Increasing the weight of these elements, *Sm_P* and *Sm_S*, has a flattening effect upon the resulting anomalies. The block which controls the amplitude of the model (equations (1e) and (1f)) has a diagonal structure with only one element in each equation and zero values in the data vector. *Re_P* and *Re_S* are the coefficients for the amplitude adjustment (regularization parameters).

[23] Determination of all the coefficients for the simultaneous inversion is a fairly crucial and delicate problem. In this study we propose an approach based on synthetic modeling (section 5.4) which provides optimum values for the parameters and realistic estimations for the velocity anomaly deviations. We also present the trade-off curves which give some additional estimates for the free parameter values (section 4.2).

[24] The resulting matrix is inverted using the LSQR method [*Paige and Saunders*, 1982*; van der Sluis and van der Vorst*, 1987]. The number of LSQR iterations providing a satisfactory convergence was 50 in our case.

[25] After performing the inversion, the velocity anomalies are recomputed in a 3-D regular grid and then added to the basic velocity model used for the next iteration which comprises steps 2, 4 and 5. In total, we have performed five iterations.

3.3. Inversion for *Vp* and *Vp/Vs* Ratio

[26] *Vp/Vs* ratio, or Poisson coefficient, is an important parameter in investigating a rock's petrophysical state. However, when *Vp* and *Vs* are obtained independently, their perturbations are strongly affected by the values of regularization parameters, whose definition is fairly ambiguous. Therefore simple division of *Vp* by *Vs* values does not necessarily provide a robust *Vp/Vs* ratio. That is why we perform both kinds of inversion: for *Vp* and *Vs*, and for *Vp* and *Vp/Vs* ratio.

[27] We developed an algorithm for *Vp* and *Vp/Vs* inversion with the main peculiarity that the matrix elements are computed along *P* and *S* raypaths. The algorithm was designed using node parameterization, as for the case of *Vp* and *Vs* inversion described above. The grids for *Vp* and $X = Vp/Vs$ are constructed according to the density of *P* and *S* rays, respectively, and do not necessarily coincide with each other.

[28] For variations of *Vp, X* and source parameters (*h*) we compose the following system of linear equations:

$$A_{ik}dv_k^p + Edh = dt_i^p \tag{2}$$

$$B_{ik}dv_k^p + CdX_m + \mathbf{F}dh = dt_i^{dif} \tag{3}$$

[29] Equations (1a)–(1f) are the same as for *Vp* and *Vs* inversion. Here

$$A_{ik} = \int_{\gamma_i^p} \frac{\partial t_i^p}{\partial V_k^p}(\gamma)d\gamma_i^p \tag{4}$$

is an element of the first derivative matrix and it reflects the effect of velocity variation in the *k*th node on the traveltime of the *i*th ray. Hypocentral parameter corrections ***dh***(*dx, dy, dz, dt*) are associated with the matrix elements $\boldsymbol{E}(p_x^p, p_y^p, p_z^p, 1)$ (elements of the *P* ray slowness vector in the source point).

[30] In equation (3), the data vector is represented by differential residuals, corresponding to *P* and *S* rays recorded at one station: $dt_i^{dif} = dt_i^s - dt_i^p$, and

$$B_{ik} = \frac{1}{X_k}\int_{\gamma_i^s} \frac{\partial t_i^s}{\partial V_k^s}(\gamma)d\gamma_i^s - \int_{\gamma_i^p} \frac{\partial t_i^p}{\partial V_k^p}(\gamma)d\gamma_i^p. \tag{5}$$

Derivatives $\partial t_i^s/\partial V_i^s$ and $\partial t_i^p/\partial V_k^p$ are computed along *P* and *S* rays for the nodes in the *P* model grid. X_k is a

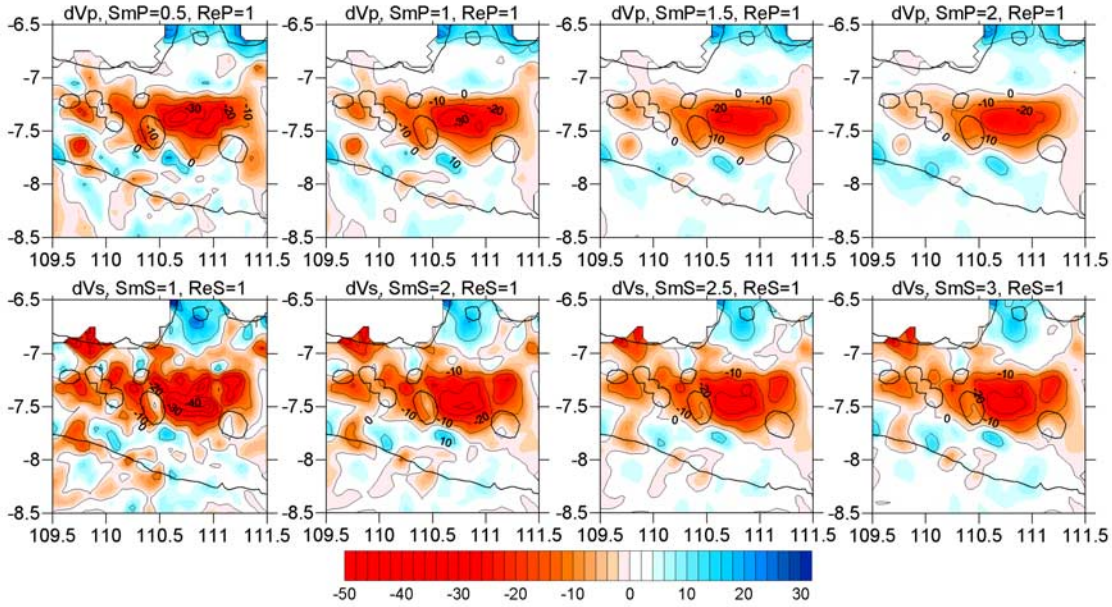

Figure 4. Some examples of the real data inversion results with different flattening parameters (*SmP* and *SmS*). Regularization parameters, which control the amplitude of the retrieved anomalies (*ReP* and *ReS*), remain unchanged. All results are represented in horizontal section at 10 km depth. Contour interval is 10%.

reference value of *Vp/Vs* ratio at the *k*th node of the *P* model grid. C_{ik} in (3) is computed as:

$$C_{ik} = -\frac{V_m^s}{X_m} \int_{\gamma_i^s} \frac{\partial t_i^s}{\partial V_m^s}(\gamma) d\gamma_i^s . \tag{6}$$

[31] Derivative $\frac{\partial t_i^s}{\partial V_m^s}$ is computed along *S* ray for the nodes in the *S* model grid. X_m and V_m^s are reference values of *Vp/Vs* ratio at the *m*th node of the *S* model grid. Hypocentral parameter corrections ***dh***(*dx, dy, dz, dt*) in (3) are associated with the matrix elements $\boldsymbol{F}(p_x^s - p_x^p, p_y^s - p_y^p, p_z^s - p_z^p, 0)$.

[32] After inversion, the distribution of *Vp*/*Vs* ratio is converted to a *Vs* model, and the relocation of sources is performed according to the algorithm described in section 3.2.

4. Results of Tomographic Inversion

4.1. Distribution of Events

[33] Final locations of the sources after five iterative inversion steps are shown in Figure 3, in map view and projected to a cross section along direction of subduction. It can be seen in the cross section that the events line up along the Benioff zone in a 30–40 km thick layer. They indicate variable dipping angle of the slab. For the first 150 km from the trench (50–250 km in the profile A-B) the slab appears to be almost horizontal. From 250 km to 450 km along

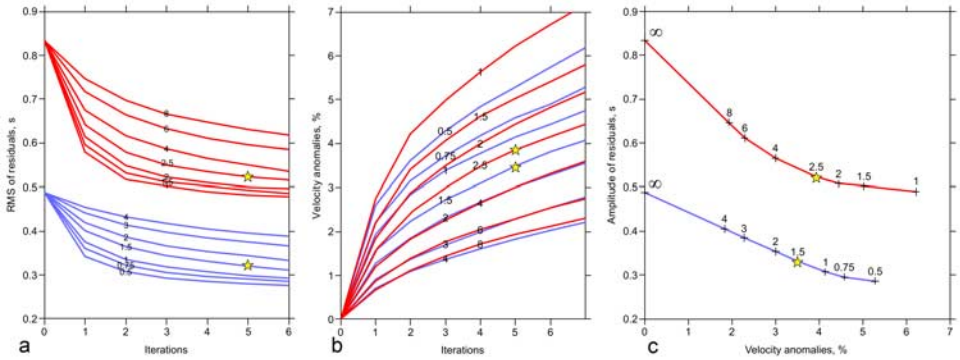

Figure 5. Effect of flattening and number of iterations on the RMS of the residuals and amplitudes of *P* and *S* models. In all plots, results for *P* and *S* models are depicted in blue and red, respectively. Numbers on curves show the values of flattening coefficients. Yellow stars indicate parameter values in the main model. (a) RMS reduction during six iterations. Zero iteration corresponds to the residuals after source location in 1-D reference model. (b) Amplitude deviation during seven iterations. (c) Trade-off curves for inversion results after five iterations.

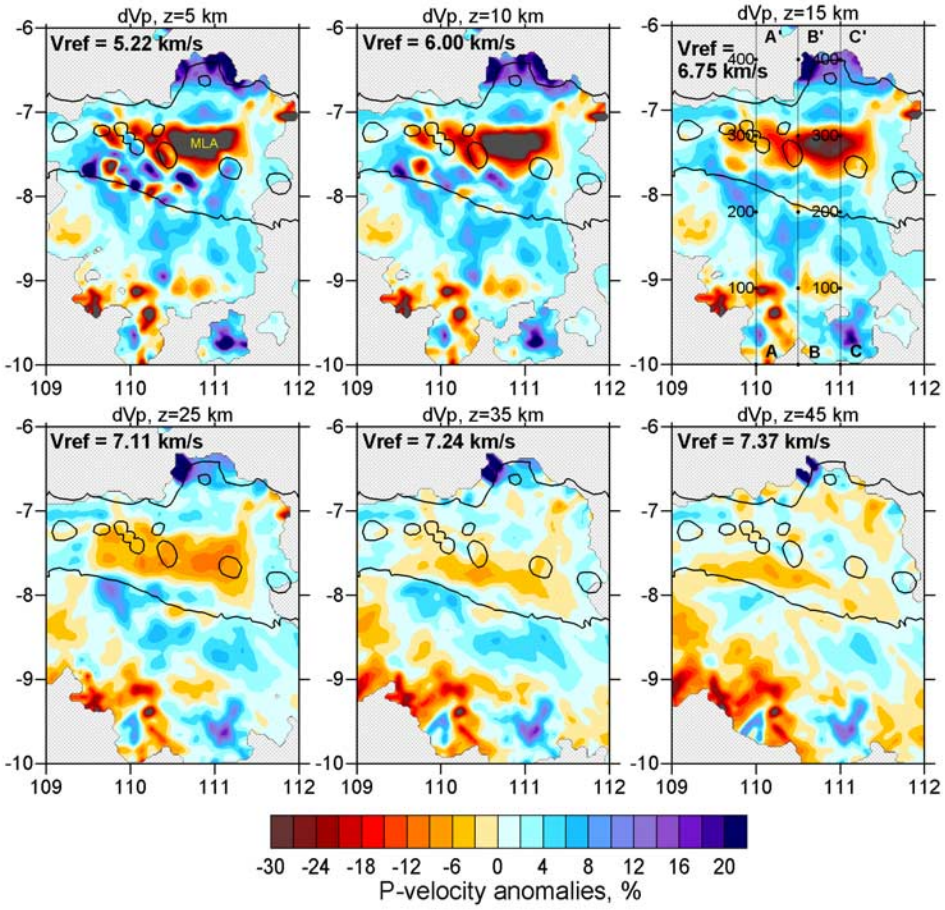

Figure 6. *P* velocity anomalies, in percent, with respect to the 1-D average velocity model, obtained as a result of tomographic inversion of real data. Base line shows the coast of Java and position of the main volcanic complexes, same as in Figure 1.

profile A-B, the dipping angle of the slab is about 45°. We do not yet have information about the sources from the deepest cluster at 600 km depth, but using the data from the ISC catalogue [*ISC*, 2001] we can estimate the further shape of the slab. In the depth interval from 250 to 600 km, the slab inclination becomes rather steep, ~70°.

[34] Slab related events in the depth interval between 40 and 130 km show a rather clear double seismic zone with dipping angle of about 45°. The thickness of this double seismic zone appears to be 20–30 km. It is important to note that spacing of the doubled seismic zone tends to decrease with the depth. Similar doubled seismicity zones with spacing of ~30 km have been observed at other subduction zones [e.g., *Nakajima et al.*, 2001]. It is presumed that the intermediate depth events are related to phase transition of blueshist to eclogite [*Peacock*, 1993, 2001]. The double seismic zone may be related to the isotherms in the subducted oceanic slab.

4.2. Amplitude of Velocity Anomalies and RMS of Residuals

[35] As was mentioned above, free inversion parameters (number of iterations, flattening and regularization coefficients) strongly affect the amplitude and sharpness of the retrieved anomalies. We have inverted for dozens of models with different free parameter sets. Some of them are presented in Table 2 with indications of values of deviations, amplitudes, and variance reduction. The role of the flattening parameters (*SmP* and *SmS*) is demonstrated in Figure 4. We present a series of inversions with the flattening parameter varying from 0.5 to 2, for *P* model and from 1 to 3, for *S* model. It can be seen that such variations cause significant change in the amplitude of the prominent negative anomaly, from ~40% to ~25% for *P* model and from ~50% to ~30%, for *S* model.

[36] Figure 5 shows the relationships between the deviation of retrieved anomalies, RMS of the residuals and values of flattening parameters after different iterations. The graphs represent inversion results for seven different flattening parameters using seven iterations. The RMS of the residuals (Figure 5a) is computed just after the source location in each iteration. In iteration 0 the RMS corresponds to the residuals after source location in the 1-D reference model. A plot of amplitude deviation versus iterations is presented in Figure 5b. It can be seen that after three iterations, the amplitude increased almost linearly for all flattening parameters. The graphs in Figure 5 show that the amplitude of the retrieved model can be controlled both with regularization coefficients and number of iterations. For example, the *P* model obtained after two iterations with smoothing

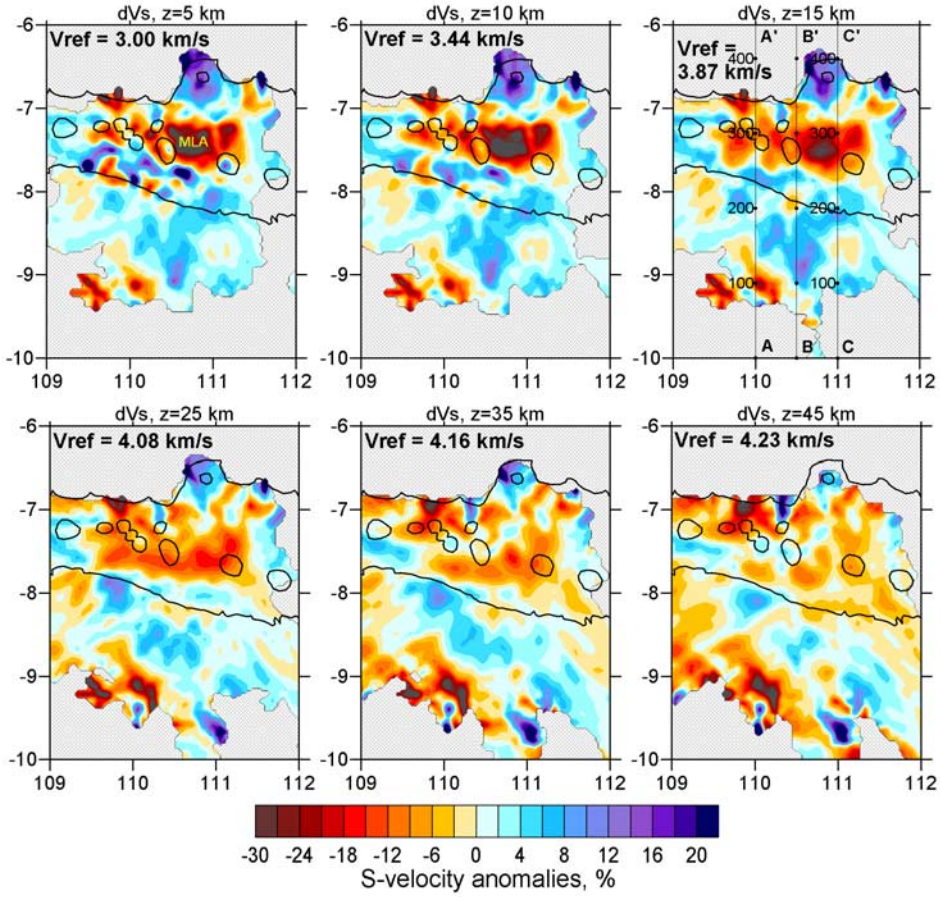

Figure 7. Same as Figure 4, but for *S* velocity anomalies.

coefficient 1.5 is similar to a model obtained with smoothing 4 after 7 iterations. However, it is clear that moving with small steps at each iteration would be more consistent with the assumption of linear inversion. For the main model we fixed 5 iterations as a compromise between calculation time and linearity condition. For this number of iterations we searched for optimum values of flattening and regularization coefficients based on the trade-off curves presented in the next paragraph and synthetic test shown in section 5.4.

[37] It should be noted that the remnant residuals for the final results are relatively strong (~0.3 s, for *P* data and ~0.5, for *S* data). These values roughly reflect the noise level in the data, which cannot provide a coherent solution. At the same time, our picking error estimates are much smaller. In particular, in most cases the *P* arrivals were very clear, and the average picking accuracy was less than 0.2 s. For *S* arrivals the difference in record quality was much stronger, but on average, picking accuracy was surely less than 0.5 s. We suppose that the remnant residuals can partially be due to some features of the true velocity distribution in the Earth, which cannot be taken into account by our model. One of them might be anisotropy, which may be strong in this highly heterogeneous area. Another explanation can be related to the existence of some small and contrasting low-velocity anomalies in the uppermost crust (e.g., 0.5–3 km size and 40–60% amplitude), which are below the resolution capacity of our inversion scheme. Theoretically they can produce a noncoherent signal which causes such strong remnant residuals after inversion.

[38] It can be seen from the curves presented in Figure 5 that the definition of flattening parameters and number of iterations, which affect the amplitude and smoothness of the retrieved anomalies, is very ambiguous. Many authors [e.g., *Eberhart-Phillips*, 1986] suggest that the key for determination of the free parameters for inversion is a trade-off curve of the model amplitude versus RMS of the residuals for various flattening parameters. In Figure 5c we present the trade-off curves for *P* and *S* models which correspond to the solutions after 5 iterations. It is presumed that the best solution corresponds to the point of maximum curvature of the curve (1.5, for *P* and 2.5, for *S* model in our case). However, in our opinion, only presenting trade-off curves, in order to define the free parameters, is not sufficiently convincing. In section 5.4 we present the results of synthetic modeling based on reconstruction of a velocity model which was obtained after real data inversion. It will be shown that this test can be used to determine free inversion parameters and realistic values of the retrieved anomalies.

4.3. Distribution of *P* and *S* Velocity Anomalies

[39] On the basis of different estimates, we conclude that the most reliable model is "1.5-2.5-1-1", which is presented in Table 2 and in Figure 4. Figures 6–8 show *Vp* and *Vs* anomalies for this model in vertical and horizontal sections.

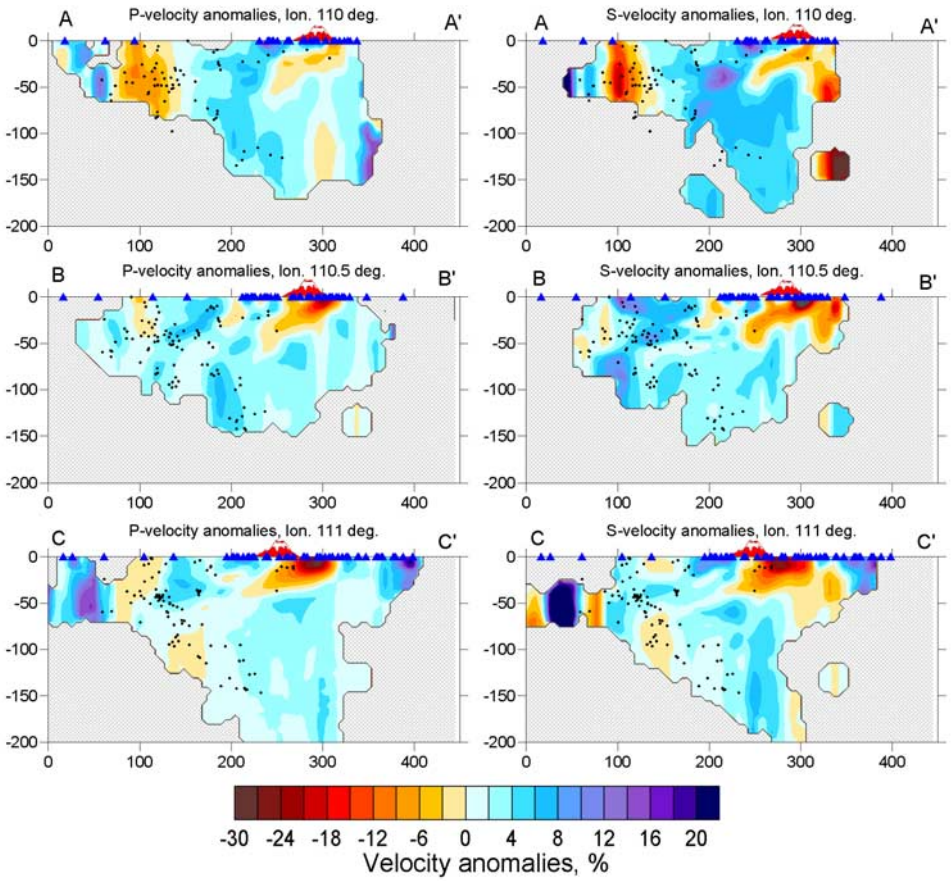

Figure 8. *P* and *S* velocity anomalies obtained from the real data inversion in three vertical sections. Position of the sections is shown in Figures 4 in the map for 15 km depth. Black dots show position of the relocated sources within 30 km of the profile. Blue triangles are the stations projected to the profile.

Here we only show the relative velocity anomalies in per cent with respect to the reference model described earlier. As we have already mentioned, we had little a priori information about absolute velocities in the study region; hence the reference model was fixed mostly arbitrarily, especially for *S* velocity. Therefore, in our case, showing the absolute velocities makes no sense. At the same time, as will be shown in section 4.6, reconstruction of relative anomalies even in highly heterogeneous areas is fairly stable and does not depend very much on the reference model. The presented results are obtained by summation for four models obtained independently in four differently oriented grids. The velocity perturbations are only shown if the distance to the nearest parameterization node is less than 10 km. Since the nodes are placed according to the ray density and distributed only in areas with sufficient ray coverage, results are shown for well resolved parts of the study volume.

[40] The first striking feature of the resulting images is the almost perfect correlation of *P* and *S* anomalies in the crust, which is not prescribed by our inversion technique (as, for example, in case of inversion for *P* and *P*/*S* ratio). In the upper mantle, the correlation between *P* and *S* models is less clear. They might be caused by lower reliability of features in the uppermost mantle compared to crustal structures.

[41] In sections at crustal depths, the prominent feature is a strong low-velocity anomaly (Merapi-Lawu Anomaly (MLA)) with 30% amplitude in *P* model and 36%, in *S* model. The shape of MLA is practically identical in the *P* and *S* models. It can be seen that this anomaly fills the areas between the main volcanic complexes. The largest part of this anomaly is located between the alignment of Merapi-Merbaru volcanoes (for short, Merapi complex) and Lawu volcano. The second, smaller part is between Merapi complex and the Sumbing-Sumdoro-Dieng volcanic chain (for short, Sumbing complex). The active volcanoes themselves seem to be located around this anomaly, above a relatively higher-seismic velocity zone in the crust. In the vertical sections, it can be seen that the MLA is inclined in shape and dips southwards. The most active volcanoes (Sumbing, Merapi and Lawu) are located just above the edge of the contact between this anomaly and the high-velocity fore arc. The vertical sections show that the MLA prolongs into the upper mantle. The reliability of this feature is tested by one of the synthetic tests described in section 5.

[42] In the fore arc, between the southern coast of Java and the volcanic arc, the crust appears to be highly heterogeneous. This could be due to alternation of highly deformed low-velocity limestone massifs and Cenozoic gabbroic intrusions. However, in most parts, the link between geology and tomographic images is not clear,

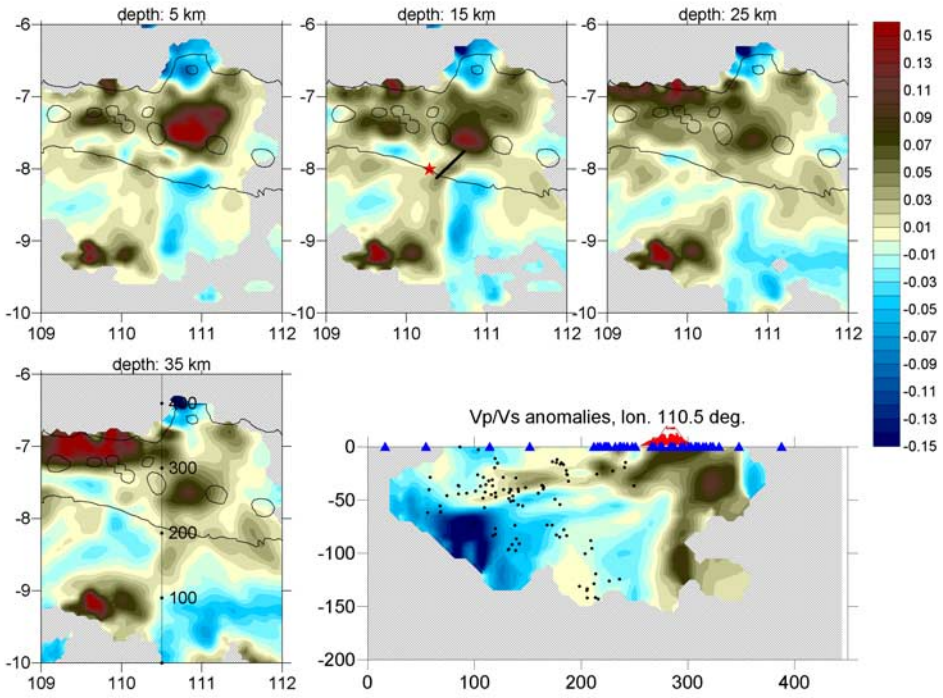

Figure 9. Horizontal sections and one vertical profile showing *Vp*/*Vs* ratio anomalies obtained after inversion for *Vp* and *Vp*/*Vs*. The values are given with respect to 1.74, a constant value in the reference model. Red star indicates position of the Java M_w = 6.3 earthquake (27 May 2006). Black line at 15 km depth indicates possible boundary between two crustal blocks. Position of the profile is shown in the map at 35 km depth. Blue triangles in vertical section indicate the stations.

because the main geological structures of central Java are covered with volcanic deposits.

[43] Another low-velocity anomaly in the crust is located at the SW edge of the study area. The reliability of this feature is disputable because it is located outside the position of the station network. As the checkerboard test shows (see section 5.2), we are unable to derive a detailed seismic structure in this part of the study area.

[44] We are not able to resolve high-velocity anomalies which are expected in the slab. Taking into account that the events in the Benioff zone are mainly located in the uppermost limit of the slab, and that the rays are traveling upward, it is clear that almost no relevant information about the slab structure itself was provided. In addition, trade-off between source parameters and velocity model prevented reliable retrieval of the velocity model in the Benioff zone.

4.4. Inversion Results for *Vp* and *Vp*/*Vs*

[45] We have performed inversions for *Vp* and *Vp*/*Vs* ratio according to the algorithm described in section 3.3 using five iterations. Here we show the distribution of the resulting *Vp*/*Vs* perturbations with respect to the reference value, 1.74 (Figure 9). The images of *Vp* and *Vs* anomalies derived after inversion for *Vp* and *Vp*/*Vs* are very similar to those after direct inversion for *Vp* and *Vs* (section 4.3).

[46] As for the *Vp* and *Vs* models (section 4.3), the most prominent crustal feature is a strong anomaly of higher *Vp*/*Vs* ratio in the MLA. For example, in the center of the MLA at 10 km depth, the *Vp*/*Vs* ratio reaches the value of about 1.9. This corresponds to *Vp* = 4.39 km/s (−26% deviation from the reference model) and *Vs* = 2.34 km/s (−32%). Such strong anomalies of seismic velocity and Poisson ratio in the MLA are probable indicators of high-fluid content and partial melting in the crust. This feature is discussed in more details in section 6.

[47] In the fore arc, south of Merapi, we observe a clear S-N oriented boundary between higher and lower values of *Vp*/*Vs* ratio. This feature can hardly be recognized in seismic velocity images. It is important to note that in the coastal area this boundary passes through the epicenter of the recent Java M_w = 6.3 earthquake (26 May 2006, (UTC)). It is probable that this represents a contact zone between two blocks of different petrophysical properties, where maximum of stresses could be accumulated.

[48] In the sections below 25 km depth, corresponding to the uppermost mantle, the MLA-related anomaly of *Vp*/*Vs* ratio is still visible, but it is much weaker and slightly shifted southward. The strongest feature at these depths is an anomaly with high *Vp*/*Vs* value, which is located north of the Slamet and Sumbing volcanic complexes. Here low-velocity *S* anomalies coexist with positive *P* anomalies. However, this zone is located at the edge of the resolution area and therefore could be due to artifacts related to the trade-off between source location and velocity model. The same applies to the anomaly with higher *Vp*/*Vs* ratio, which is observed in all depth sections at the southern edge of the study area. It can also be due to boundary effect and

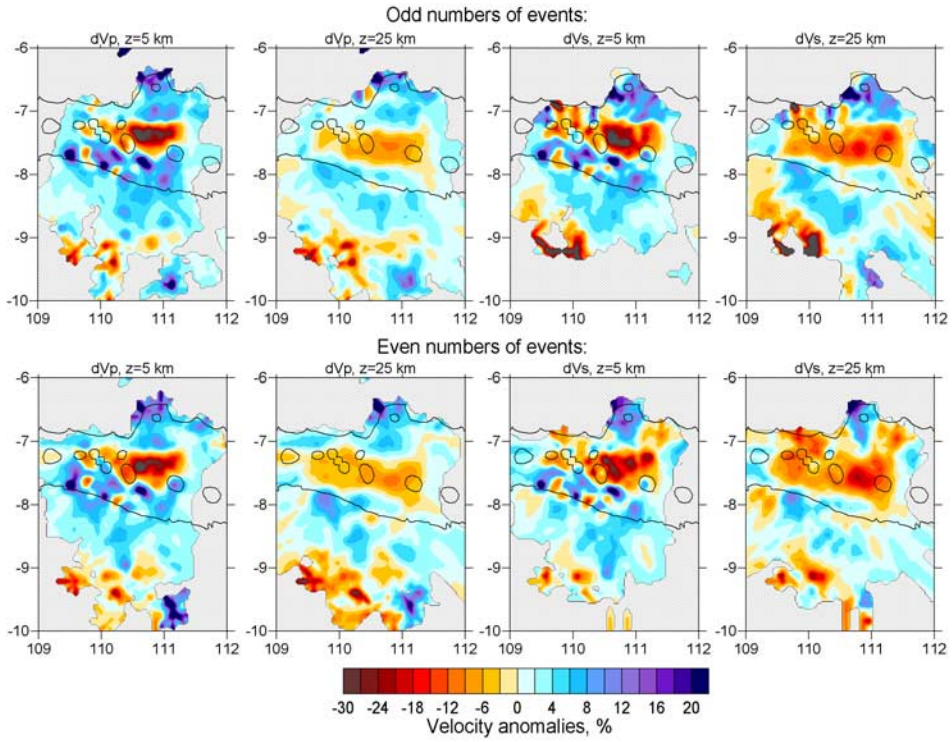

Figure 10. *P* and *S* velocity anomalies obtained from the independent inversion of two data subsets with (top) odd and (bottom) even numbers of events.

uncertainties of source locations. Therefore reliability of these two features is questionable.

4.5. Inversion of Two Data Subsets

[49] The relatively high RMS values (0.307 s, for *P* data and 0.507 s, for *S* data) obtained after five iterations of inversion, suggest that unexplained factors still play an important role. Theoretically, it is possible that these remnant residuals are due to some random factors which can produce artifacts even in areas with high resolution. To check it, we perform the following test. The contribution of random noise to the resulting images can be estimated by performing independent inversions of independent data subsets. In this test, the whole data set is divided into two subsets: with odd and even numbers of events. The structure of the processing algorithm and all tuning parameters remain the same as in the case of inverting of the entire data set.

[50] Results of inversion for *P* and *S* models for odd and even events are shown in Figure 10. The models can be compared with each other and also with the results using the entire data set (Figures 6 and 7) to show the effect of data halving on the inversion results. The results of inversion for the *P* and *S* models in the crust (for 5 km depth) show almost perfect correlation between the maps. Even small patterns, less than 30 km of lateral size, are reliably reconstructed in both models. This gives us quite high confidence for the obtained *P* and *S* velocity models in the crust. For the uppermost mantle (for 25 km depth) the correlation is not as good as in the crust. However, the main patterns are generally visible in both models. In the deeper sections the correlation becomes poorer. This might be caused by the random noise effects and trade-off between velocity model and source locations.

[51] From this test we can conclude that the remnant residuals are mainly not due to random noise. Their nature still remains unclear to us. These residuals could be related to some regular features which are not taken into account by our model. It might be, for example, that strong small velocity patterns which cannot be resolved by our model, still have an effect on traveltimes. Possible structures which might cause such effect are discussed in section 6.

4.6. Effect of the Reference Model on the Result

[52] As we have already mentioned in section 3.1, the initial 1-D model for the *S* velocity was obtained from the *P* velocity distribution by simple multiplication with a

Table 3. Standard Deviations of P and S Residuals and Variance Reductions of Tomographic Inversions in the Velocity Models With Different Vp/Vs Ratios

	Standard Deviation				Variance Reduction	
	Before 1 Iteration		After 5 Iterations		After 5 Iterations	
Vp/Vs Ratio	dtp	dts	dtp	dts	dtp	dts
1.70	0.508	0.849	0.316	0.512	37.8	39.7
1.72	0.495	0.839	0.313	0.508	36.7	39.4
1.74	0.488	0.833	0.307	0.507	37.1	39.1
1.76	0.492	0.839	0.315	0.516	35.9	38.5
1.78	0.497	0.844	0.311	0.512	37.3	39.3
1.78	0.507	0.856	0.316	0.522	37.6	39.1

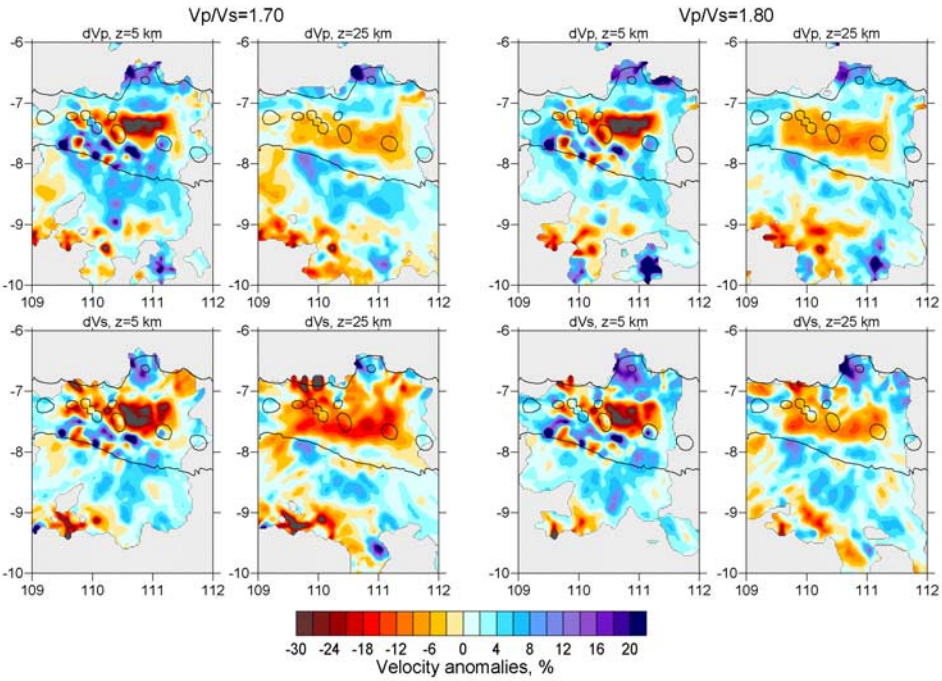

Figure 11. *P* and *S* velocity anomalies obtained from the real data inversion for two reference models with (left) 1.70 *Vp*/*Vs* ratio and (right) 1.80. (top) *P* velocity anomalies; (bottom) *S* anomalies. Here we present the results for two depth levels, 5 km and 35 km. It can be seen that a change of the reference model does not significantly affect the shape of the anomalies.

constant *Vp*/*Vs* ratio. The RMS values for *P* and *S* residuals after location with one and five iterations for a series of reference models are given in Table 3. Values for the first iteration correspond to the residuals after source location in the 1-D model. RMS values after 5 iterations are presented. The reference *P* velocity initial distribution was always the same, while the *Vp*/*Vs* values changed from 1.70 to 1.80. The best initial and final RMS was derived with a ratio equal to 1.74, which was taken to calculate our main results.

[53] To show the effect of the reference model change on the resulting images of velocity anomalies, we present here the inversion results for two significantly different *Vp*/*Vs* ratios, 1.70 and 1.80 (Figure 11). This change caused a significant shift of sources. In particular, for sources at a depth of 200 km, the difference in locations was more than 20 km. At the same time, comparison of the *P* and *S* anomalies obtained for these two different models, as well as with the main results (*Vp*/*Vs* = 1.74, Figures 6 and 7), shows that they are almost equivalent. Hence two important conclusions can be drawn from this test. First, the true reference model is hardly retrievable from the local earthquakes data. Second, the absence of knowledge about the reference model does not harm the final results of relative velocity perturbations.

5. Testing

5.1. General Strategy of the Synthetic Testing

[54] Although the main resulting anomalies seem to be fairly clear, the following questions should be investigated:

[55] 1. Can we reliably determine the true amplitude of the anomalies? This is important because of a trade-off between the flattening and amplitudes of velocity variations in the inverted model.

[56] 2. Can the anomaly in the crust be due to downward smearing of strong anomalies in the uppermost layer (sediments or unconsolidated volcanic deposits)?

[57] 3. Can the anomaly in the mantle wedge be due to downward smearing of crustal anomalies?These and other questions are investigated in this section.

[58] Our algorithm allows definition of various synthetic models either as periodical anomalies in the checkerboard test or manually by drawing some shapes in vertical or horizontal sections. The traveltimes for the synthetic test are computed by 3-D ray tracing between sources and receivers corresponding to the real observation system. We add random noise with a magnitude which provides the same variance reduction as after the real data inversion. These times are the input for the whole inversion procedure, including the step 1 of absolute source location. As in the real case, searching for the source location starts from the position of a station with minimum arrival time. The values of the inversion parameters for the synthetic test are the same as those used for the real data inversion.

5.2. Checkerboard Test

[59] To evaluate the horizontal resolution of the model in different parts of the study area, we perform a checkerboard test. The initial model is represented by unlimited vertical columns of alternated positive and negative anomalies of 30 km lateral size. The amplitude of velocity contrast for both *P* and *S* models is set to ±7%. In this test, we added random noise with 0.2 and 0.5 s RMS for *P* and *S* data, respectively.

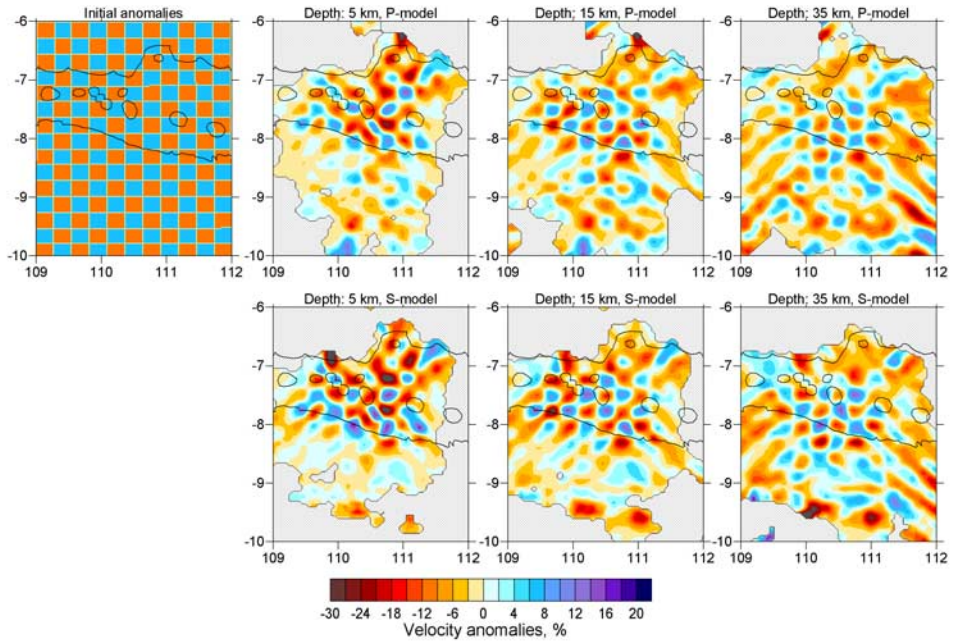

Figure 12. Result of the checkerboard test for *P* and *S* models using the real data observation system. The initial model is represented by unlimited vertical columns of alternated positive and negative anomalies. The initial anomaly (±7% amplitude) is shown in the first map. The RMS of noise is 0.15 and 0.3 s, for *P* and *S* data, respectively. The reconstruction procedure is identical to the one used in the real data inversion, including absolute location of sources.

[60] The results of the reconstruction of the *P* and *S* velocity models after five iteration steps for four differently orientated grids are shown in Figure 12. In the crust, the best resolution is achieved beneath Java, where most of the onshore seismic stations were installed. For the offshore area, the ray geometry does not provide sufficient resolution to retrieve features less than 30 km in size. This test does not corroborate reliability of the low-velocity anomaly in southwest observed in real data inversion (Figures 6 and 7).

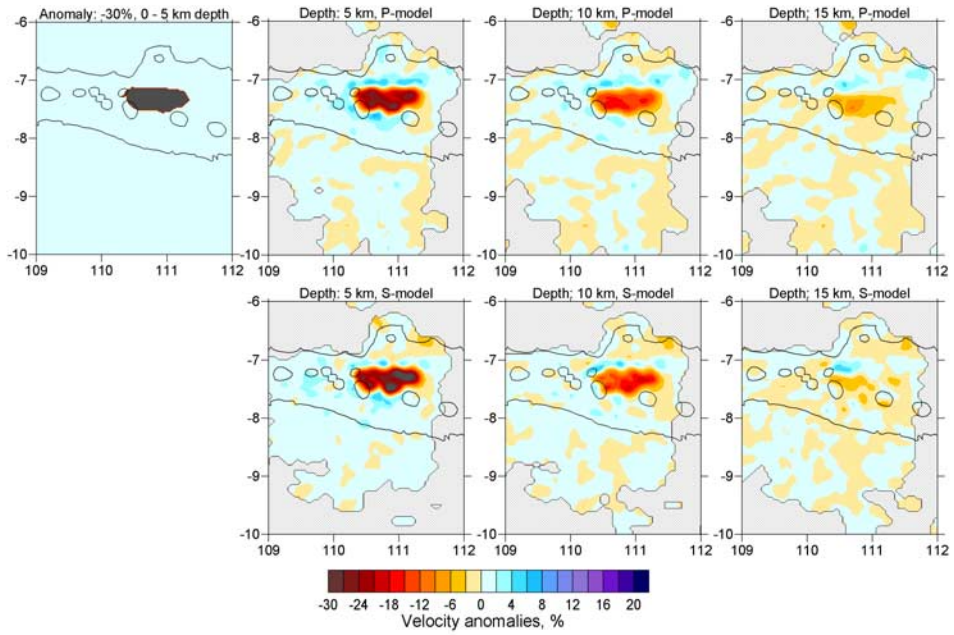

Figure 13. Synthetic test in order to investigate the effect of a strong shallow negative anomaly. An initial velocity anomaly of 30% amplitude is defined at depths between 0 and 5 km. The RMS of noise in the data is 0.1 s. The reconstruction result shows a downward smearing of the shallow anomaly; however, it is not sufficient to explain the observed MLA in the middle and lower crust.

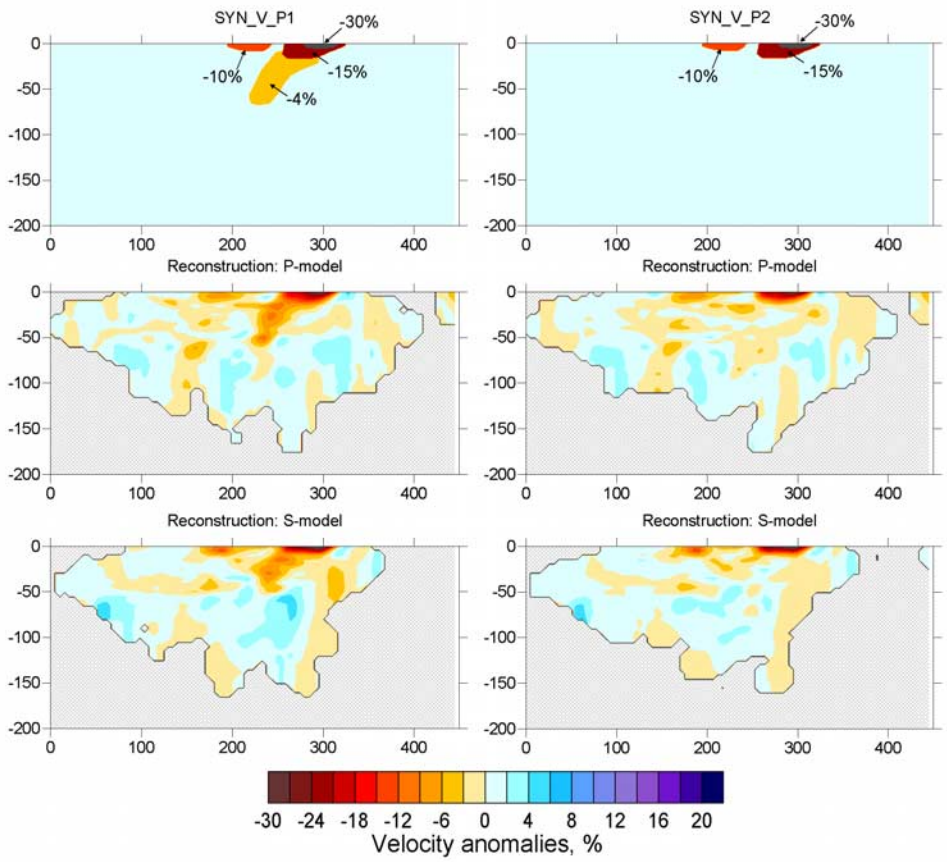

Figure 14. Synthetic test to investigate the effect of an anomaly in the uppermost mantle. Two synthetic models, with and without the mantle anomaly, are considered. (top) Values and shapes of the initial anomalies. The RMS of noise in the data is 0.1 s. (middle and bottom) Reconstruction result for *P* and *S* models, showing that these two models are clearly differentiated. Thus the anomalies observed in the upper mantle are not due to smearing of crustal anomalies.

[61] In the upper mantle, sufficient resolution is achieved only in the central part of the study area under the southern coast of Java. The vertical resolution has been investigated in other synthetic tests. Some of them are presented below.

5.3. Tests for Checking Real Situations

[62] A similar strategy as described in section 5.2 is applied for reconstruction of a series of other synthetic models. These tests aim at checking reliability of different features in the resulting model. We checked many different configurations of synthetic anomalies and noise parameters which modeled various realistic and nonrealistic situations.

5.3.1. Shallow Anomaly Effect

[63] A question which should be checked for prompt verification of the results is whether the observed low-velocity anomaly MLA in the crust is an artifact due to some near-surface factors. In Figure 13 we present the test aiming at investigating the effect of a strong shallow anomaly on the inversion results in the crust. The initial velocity anomaly with 30% amplitude is located at the position of MLA in the depth range of 0–5 km. This anomaly models sediments and unconsolidated volcanic deposits which could be expected between Merapi and Lawu volcanoes. Thickness and amplitude of this anomaly are overestimated to provide the most pessimistic estimations. Noise of 0.1 s amplitude was added to the computed synthetic residuals. The parameters and all the steps of inversion were the same as for the real data case. The reconstruction results show fairly strong downward smearing of the anomaly. At the same time, we observe a decrease of amplitudes of the retrieved anomalies with depth. At 5 km depth, the amplitude of the anomaly is larger than 15%, at 10 km depth it has ~8% and at 15 km depth it decreases to <2%. In the real data inversion, the amplitude of *P* and *S* anomalies in the crust, beneath MLA (Figures 6–8), does not vary so significantly with depth. This shows that, although the effect of smearing is quite important, the images of the real data inversion cannot be obtained merely due to an effect of near surface anomalies.

5.3.2. Test for Checking the Reliability of Anomalies in the Uppermost Mantle

[64] In the uppermost mantle we observe a low-velocity anomaly which seems to link the MLA with the seismicity cluster in the slab at about 100 km depth. Before interpreting this anomaly, it is important to check whether it is a robust feature or an artifact related to downward smearing of MLA. In order to validate this, we reconstruct two synthetic models using the same crustal anomalies, but with different upper mantle structures (homogeneous and with a 4% amplitude anomaly). Comparison of the reconstructed

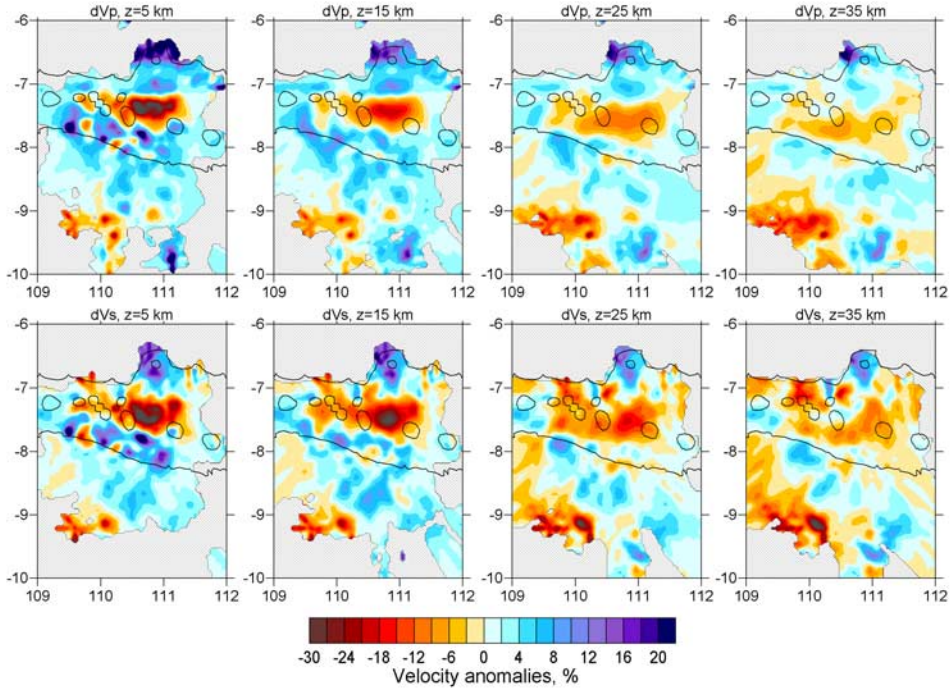

Figure 15. Test with a synthetic model constrained from the real data results. Velocity distributions obtained after inversion of real data (Figures 6–8) were used as an initial model in order to calculate synthetic traveltimes. Inversion conditions were the same as those used in real data processing. Noise with deviations of 0.2 and 0.6 s was added. The noise provided approximately the same variance reduction as in real inversion. (top) *P* and (bottom) *S* velocity anomalies reconstructed after inversion of the synthetic data.

results (Figure 14) shows that the present configuration of rays cause almost no downward smearing of the crustal anomalies. The model with an anomaly in the upper mantle is closer to the real data inversion result, and thus we suggest that a similar anomaly in the upper mantle is real.

5.4. Reconstruction of a Realistic Velocity Structure

[65] The final test aims at checking the correct definition of free inversion parameters and at evaluating the true amplitude of the anomalies. The synthetic traveltimes in this test are computed by 3-D ray tracing through a model obtained after the real data inversion (e.g., model "1.5-2.5-1-1", Table 2, Figures 6–8). All the free parameters for the synthetic inversion are identical to those used for calculation of the corresponding real data model (e.g., 5 iterations, *SmP* = 1.5, *SmS* = 2.5, *ReP* = 1, *ReS* = *1*). The amplitude of the added noise is estimated to achieve the same variance reduction as in the case of the real data inversion (e.g., 0.25 s and 0.6 s to provide ~35% and ~40% of variance reduction for *P* and *S* data respectively). We performed the test for several models, and a best fit between original and retrieved velocity distributions was achieved for the "1.5-2.5-1-1" model. For example, in case of model "3-4-1-1", the retrieved distribution is smoother than the original model and amplitudes of anomalies are lower. On the contrary, for model "0.5-1-1-1", the inversion produces some artifacts, which do not exist in the original model, and amplitudes, which are stronger than in the original model. The results for reconstruction of model "1.5-2.5-1-1" are shown in Figure 15. These maps can be compared with the original model presented in Figures 6 and 7. It can be seen that both the amplitudes and shapes of the anomalies coincide very well.

[66] Let us assume X_0 is a real velocity distribution in the Earth. Rays traveling through this velocity distribution produce the real data set D_0. Performing inversion with some set of free parameters, S_0, produces the resulting model X_1. In fact, the standard deviation of the anomalies in the obtained model, $\|X_1\|$, is not necessarily the same as $\|X_0\|$, because of the uncertainty of the free parameters definition. After performing inversion for the data computed by tracing through X_1, with the same set of free parameters as in the real data inversion, we obtain model X_2. Since the inversion conditions were absolutely identical, we can assume that:

$$\frac{\| X_1 \|}{\| X_0 \|} \approx \frac{\| X_2 \|}{\| X_1 \|}.$$

[67] In the case when the original and retrieved models are similar ($\|X_2\| \sim \|X_1\|$), one can assume that the result obtained after the real inversion with the same set of free parameters is close to the real velocity structure in the Earth ($\|X_1\| \sim \|X_0\|$). From the fact that the best fit is achieved for the "1.5-2.5-1-1" model, presented in Figures 6, 7, and 15, we can conclude that this is the best model representing the

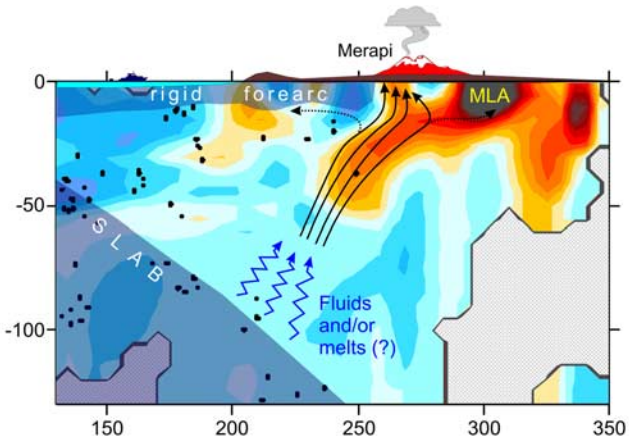

Figure 16. Interpretation of the velocity structure beneath Merapi. Background is the *S* velocity anomaly distribution in the vertical section B-B′ (Figure 8).

real velocity distribution beneath central Java among all others presented in Table 2 and Figure 4.

[68] Now we can make a grounded conclusion about the velocity amplitudes inside the MLA. In its central part, *P* and *S* anomalies reach 30% and 36% respectively. This corresponds to the *Vp*/*Vs* ratio of ∼1.9, the same as we observe in the inversion for *Vp*/*Vs* in Figure 9.

6. Discussion and Conclusions

[69] We present evidences for a very strong low-velocity anomaly, MLA, which is observed both in *P* and *S* velocities in the crust just north of Sumbing, Merapi and Lawu volcanoes. It is important to note that the volcanoes themselves appear to be located above relatively higher-velocity patterns.

[70] The amplitude of the MLA is exceptionally high, 30% for *P* model and 36% for *S* model. This value has been verified by synthetic modeling in section 5.4, which consisted in recovering results similar in all senses to the real data inversion. We showed that part of this anomaly might be caused by smearing of strong anomalies in the uppermost layer (0–5 km depth). However, our synthetic tests show that such an anomaly would not be enough to provide the high amplitudes observed down to 20–25 km depth. Therefore the deeper parts of the crust should have very low velocities as well. This has also been confirmed by active seismic studies in which the vertical smearing effect is less important [*Wagner et al.*, 2007]. It should also be noted that at stations located above this anomaly very strong attenuation of seismic signal is observed, especially in *S* waves.

[71] The nature of such a huge negative anomaly in the crust is still under discussion. It is known that sediments are very thick in this area, but we could not find any quantitative information about the thickness of the sedimentary layer. One of the possible reasons for significant *P* and *S* velocity lowering within the MLA could be high content of gas and fluids in the thick sedimentary layer. There are some evidences for gas deposits and mud volcanoes with active release of methane observed in central Java, which favor this hypothesis.

[72] On the other hand, as was shown above, amplitude of anomalies in the lower parts of the crust beneath MLA are very strong too. This can be explained by high content of fluids and partial melts throughout the whole crust between Merapi and Lawu volcanoes. The natural question arises, why most active volcanoes are observed on the southern borders of the MLA and not above its center? Why do we not observe any thermal activity above MLA? In the literature we did not find any evidences of anomalous thermal processes inside the MLA. Perhaps, the thick sediments play a sealing role and do not allow these ascending materials to reach the surface. However, in this case it would not be clear, why the active volcanoes are only located at the southernmost border of the MLA and not all around.

[73] Another possible explanation was suggested by V. R. Troll (Trinity College, University of Dublin, personal communication, 2006). It was proposed that the material in the MLA is presently at a cooling stage, which produces a rigid matrix filled with pockets of molten material. As a result, this zone should be fairly rigid and of low velocity. This would explain why the fluids and melts from the mantle wedge just beneath the MLA cannot pass directly to the surface. This hypothesis is indirectly supported by relatively strong remnant noise in the data after our inversion. One of the explanations for this fact could be the existence of relatively small bodies of contrasting material. They affect the traveltimes of seismic rays but cannot be retrieved because of the limited resolution capacity of tomographic inversion. Taking into account realistic frequencies of seismic rays from natural sources, a significant effect on the traveltime can be achieved if the anomaly size is larger than 1–2 km. On the other hand, it should be below our resolution capacity, i.e., ∼15–20 km, because otherwise we would detect them in our images and the signal would be coherent. Pockets of molten or partially molten material (2–15 km size) distributed beneath the MLA in a solid matrix might produce the characteristics we observe in this study: very strong negative *P* and *S* anomalies, a high *Vp*/*Vs* ratio, strong (but not complete) attenuation of *S* waves and a high level of noncoherent component in the residuals.

[74] In Figure 16 we show an interpretation of the velocity section passing through Merapi and propose a link between volcanism in central Java and processes in the subducted slab. We suggest that the earthquake cluster at 100 km depth is related to active release of fluids and partial melting, which is caused by a phase transition in the slab. The ascending fluids cause a decrease in the melting temperature of material in the mantle wedge [*Poli and Schmidt*, 1995]. Above 60 km depth we observe an inclined negative anomaly, which can be caused by partial melting. When the fluids and diapires reach the bottom of the rigid fore arc, they are not able to pass through it and follow its bottom contour. Fluids probably behave in the same manner beneath the MLA. As a result of such a migration from beneath the fore arc and MLA, the highest concentration of melts would occur at the boundary between them. This is the most probable location for active volcanism that we observe today.

[75] We should mention that Muria volcano at the northern coast of Java is located above a large high-velocity zone with low *Vp*/*Vs* ratio. This might be an indicator of low

temperature in the crust. It is not connected to the MLA, which apparently plays some role in feeding the active volcanoes of central Java. Therefore we would not expect any volcanic activity of the Muria volcano in the nearest future.

[76] Some links between the retrieved seismic anomalies at shallow depth level and surface tectonics might be found. In particular, a low-velocity anomaly observed SSW of Merapi correlates with a limestone mountain range. The high-velocity patterns in the fore arc relate to magmatic outcrops dated at about 20–30 Ma. However, in general, it is hard to compare the surface geology with our results for most of the study area, because it is entirely covered by recent sediments and volcanic deposits.

[77] There is a good correlation between the distribution of velocity anomalies in the crust and gravity anomalies [*Untung and Sato*, 1978*; Smith and Sandwell*, 1997]. High-velocity seismic anomalies in the fore arc correspond to gravity highs, and low-velocity MLA is located at a gravity low. The latter can be explained by a density deficit in the MLA, probably caused by increased temperature, fluids, and perhaps pockets filled with partial molten material.

[78] The low-velocity anomaly at the SW edge of the study area is also generally confirmed by synthetic tests. This anomaly could reflect tectonic features like compressional fracturing and thickening of the crust just behind the Java trench. This result is corroborated by preliminary results of active seismic offshore profiling of the area between the trench and Java, carried out as part of the MERAMEX project (A. Wittwer, IFM-GEOMAR, personal communication, 2005).

[79] As a summary we can point out the main results of this study:

[80] 1. Earthquakes locations on the basis of high-quality local seismological observations clearly mark the shape of the slab in the Benioff zone beneath the central Java. Within about 150 km from the trench, the slab is almost horizontal. Between 150 and 250 km distance from the trench the dip angle of subduction is estimated to be $\sim$45°. Further to the north, the slab dips much steeper, with an angle of $\sim$70°.

[81] 2. The hypocenter distribution of local seismicity delivers evidence for a double seismic zone in the slab at 80–150 km depth.

[82] 3. We have found an exceptionally strong velocity anomaly in the crust between Merapi and Lawu volcanoes, with amplitude of 30% for *P* and 36% for *S* model, and with a high Poisson ratio, $Vp/Vs = 1.9$. We suppose that this anomaly is related to an area with high content of fluids and melts in the crust. It can play a role in feeding the active volcanoes in central Java.

[83] 4. In the upper mantle an inclined low-velocity zone beneath the MLA probably reflects the migration paths of fluids and partial melts from the slab.

[84] **Acknowledgments.** This research was founded by the Federal Ministry of Education and Research (BMBF) within the special program GEOTECHNOLOGIEN and the GeoForschungsZentrum Potsdam (GFZ). Essential support of the project was provided by the Volcanological Survey of Indonesia (VSI) Bandung, the Volcanological Technologicy Research Center (BPPTK) Yogyakarta, the Gadjah Mada University (UGM) Yogyakarta, Institut Teknologi Bandung (ITB) Bandung, and the Meteorological and Geophysical Agency (BMG) Jakarta. We would like to thank all Indonesian and German colleagues and students participating in the fieldwork. This work would not have been possible without kind participation of Indonesian local authorities and other people who facilitate the setup and maintenance of such a large seismological network. We are also very grateful to Alexey Emanov for helping us speed up the picking of seismograms. Instruments were provided by the Geophysical Instrument Pool Potsdam (GIPP), the Christian Albrecht Universität, Kiel, and the IFM-GEOMAR, Kiel.

References

Beauducel, F., and F. H. Cornet (1999), Collection and three-dimensional modeling of GPS and tilt data at Merapi volcano, Java, *J. Geophys. Res.*, *104*, 725–736.

Bijwaard, H., W. Spakman, and R. Engdahl (1998), Closing the gap between regional and global travel time tomography, *J. Geophys. Res.*, *103*, 30,055–30,078.

Camus, G., A. Gourgaud, P.-C. Mossand-Berthommier, and P. M. Vincent (2000), Merapi (central Java, Indonesia): An outline of the structural and magmatological evolution, with a special emphasis to the major pyroclastic events, *J. Volcanol. Geotherm. Res.*, *100*, 139–163.

DeMets, C., R. Gordon, D. Argus, and S. Stein (1990), Current plate motions, *Geophys. J. Int.*, *101*, 425–478.

Eberhart-Phillips, D. (1986), Three-dimensional velocity structure in northern California Coast Ranges from inversion of local earthquake arrival times, *Bull. Seismol. Soc. Am.*, *76*, 1025–1052.

Gertisser, R., and J. Keller (1998), The Holocene volcanic activity and magmatic evolution of Merapi volcano, central Java: Constraints from stratigraphic, chronologic and geochemical data, in *Decade-Volcanoes Under Investigation, 1st Merapi-Galeras Workshop, Potsdam June 25, 1998*, edited by J. Zschau and M. Westerhaus, *Mitt. III/1998*, pp. 15–19, *Dtsch. Geophys. Ges.*, Potsdam, Germany.

Gertisser, R., and J. Keller (2003), Temporal variations in magma composition at Merapi Volcano (central Java, Indonesia): Magmatic cycles during the past 2000 years of explosive activity, *J. Volcanol. Geotherm. Res.*, *123*, 1–23.

Gorbatov, A., and B. L. N. Kennett (2003), Joint bulk-sound and shear tomography for Western Pacific subduction zones, *Earth Planet. Sci. Lett.*, *210*, 527–543.

Gossler, J. (2000), Teleseismic observations at Merapi Volcano, Indonesia, in *Decade-Volcanoes Under Investigation, 2nd Merapi-Galeras Workshop, Hannover, November 10, 1999,* edited by B. Buttkus, S. Greinwald, and J. Ostwald, *Mitt. IV/2000*, pp. 17–22, *Dtsch. Geophys. Ges.*, Potsdam, Germany.

Graeber, F., and G. Asch (1999), Three-dimensional models of *P*-wave velocity and *P*-to-*S* ratio in the southern central Andes by simultaneous inversion of local earthquake data, *J. Geophys. Res.*, *104*, 20,237–20,256.

Haberland, C., and A. Rietbrock (2001), Attenuation tomography in the western central Andes: A detailed insight into the structure of a magmatic arc, *J. Geophys. Res.*, *106*, 11,151–11,167.

Hoffmann-Rothe, A., O. Ritter, and V. Haak (2001), Magnetotelluric and geomagnetic modelling reveals zones of very high electrical conductivity in the upper crust of central Java, *Phys. Earth Planet. Inter.*, *124*, 131–151.

International Seismological Centre (ISC) (2001), *Bulletin Disks 1-9* [CD-ROM], Thatcham, U.K.

Kennett, B. L. N., E. R. Engdahl, and R. Buland (1995), Constraints on seismic velocities in the Earth from traveltimes, *Geophys. J. Int.*, *122*, 108–124.

Kissling, E., W. Ellsworth, D. Eberhart-Phillips, and U. Kradolfer (1994), Initial reference models in local earthquake tomography, *J. Geophys. Res.*, *99*, 19,635–19,646.

Koulakov, I., and S. Sobolev (2006), Moho depth and three-dimensional *P* and *S* structure of the crust and uppermost mantle in the Eastern Mediterranean and Middle East derived from tomographic inversion of local ISC data, *Geophys. J. Int.*, *164*, 218–235.

Koulakov, I., S. V. Sobolev, and G. Asch (2006), P- and S-velocity images of the lithosphere-asthenosphere system in the Central Andes from local-source tomographic inversion, *Geophys. J. Int.*, *167*, 106–126.

Maercklin, N., C. Riedel, W. Rabbel, U. Wegler, B.-G. Lühr, and J. Zschau (2000), Structural investigation of Mt. Merapi by an active seismic experiment, *Decade-Volcanoes Under Investigation, 2nd Merapi-Galeras Workshop, Hannover, November 10, 1999,* edited by B. Buttkus, S. Greinwald, and J. Ostwald, *Mitt. IV/2000*, pp. 13–16, *Dtsch. Geophys. Ges.*, Potsdam, Germany.

Müller, A., and V. Haak (2004), 3-D modeling of the deep electrical conductivity of Merapi volcano (central Java): Integrating magnetotellurics, intuction vectors and the effects of steep topography, *J. Volcanol. Geotherm. Res.*, *138*, 205–222.

Müller, R. D., W. R. Roest, Y.-J. Royer, L. M. Gahagan, and J. G. Sclater (1997), Digital isochrons of the world's ocean floor, *J. Geophys. Res.*, *102*, 3211–3214.

Müller, M., A. Hördt, and F. M. Neubauer (2002), Internal structure of Mount Merapi, Indonesia, derived from long-offset transient electromagnetic data, *J. Geophys. Res.*, *107*(B9), 2187, doi:10.1029/2001JB000148.

Nakajima, J., T. Matsuzawa, A. Hasegawa, and D. Zhao (2001), Three-dimensional structure of *Vp*, *Vs*, and *Vp*/*Vs* beneath northeastern Japan: Implications for arc magmatism and fluids, *J. Geophys. Res.*, *106*, 21,843–21,858.

Paige, C. C., and M. A. Saunders (1982), LSQR: An algorithm for sparse linear equations and sparse least squares, *Trans. Math. Software*, *8*, 43–71.

Peacock, S. M. (1993), The importance of blueshist-eclogite dehydration reactions in subducting oceanic crust, *Bull. Seismol. Soc. Am.*, *105*, 684–694.

Peacock, S. M. (2001), Are the lower planes of double seismic zones caused by serpentine dehydration in subducting oceanic mantle, *Geology*, *29*, 299–302.

Poli, S., and M. W. Schmidt (1995), H_2O transport and release in subduction zones: Experimental constrains on basaltic and andesitic systems, *J. Geophys. Res.*, *100*, 22,299–22,314.

Purbawinata, M., A. Ratdomopurbo, A. Sinulingga, I. K. Sumarti, and S. Suharno (1997), Merapi Volcano—A guide book, 64 pp., Volcanol. Surv. of Indonesia, Bandung.

Ratdomopurbo, A., and G. Poupinet (2000), An overview of the seismicity of Merapi volcano (Java, Indonesia), 1983–1994, *J. Volcanol. Geotherm. Res.*, *100*, 193–214.

Schurr, B., G. Asch, A. Rietbrock, R. Trumbull, and C. Haberland (2003), Complex patterns of fluid and melt transport in the central Andean subduction zone revealed by attenuation tomography, *Earth Planet. Sci. Lett.*, *215*, 105–119.

Simkin, T., and L. Siebert (1994), *Volcanoes of the World: A Regional Directory, Gazetteer, and Chronology of Volcanism During the Last 10,000 Years*, 2nd ed., 368 pp., Geoscience Press, Tucson, Ariz.

Smith, W. H. F., and D. T. Sandwell (1997), Global seafloor topography from satellite altimetry and ship depth soundings, *Science*, *277*, 1957–1962.

Tiede, C., A. G. Camacho, C. Gerstenecker, J. Fernández, and I. Suyanto (2005), Modeling the density at Merapi volcano area, Indonesia, via the inverse gravimetric problem, *Geochem. Geophys. Geosyst.*, *6*, Q09011, doi:10.1029/2005GC000986.

Um, J., and C. Thurber (1987), A fast algorithm for two-point seismic ray tracing, *Bull. Seismol. Soc. Am.*, *77*, 972–986.

Untung, M., and Y. Sato (1978), *Gravity and Geological Studies in Java, Indonesia*, *Spec. Publ. 6*, 207 pp., Geol. Surv. of Indonesia, Bandung.

Van der Sluis, A., and H. A. van der Vorst (1987), Numerical solution of large, sparse linear algebraic systems arising from tomographic problems, in *Seismic Tomography: With Applications in Global Seismology and Exploration Geophysics*, edited by G. Nolet, pp. 49–83, D. Reidel, Norwell, Mass.

Wagner, D., I. Koulakov, W. Rabbel, B.-G. Luehr, A. Wittwer, H. Kopp, M. Bohm, and G. Asch (2007), Joint inversion of active and passive seismic data in central Java, *Geophys. J. Int.*, *164*(1), 218–235, doi:10.1111/j.1365-246X.2005.02791.x.

Wassermann, J., M. Ohrnberger, F. Scherbaum, J. Gossler, and J. Zschau (1998), Continuous measurements at Merapi volcano (Java, Indonesia) using a network of small-scale seismograph arrays, in *Decade-Volcanoes Under Investigation, 1st Merapi-Galeras Workshop, Potsdam June 25, 1998*, edited by J. Zschau and M. Westerhaus, *Mitt. III/1998*, p. 81, *Dtsch. Geophys. Ges.*, Potsdam, Germany.

Wegler, U., and B.-G. Lühr (2001), Scattering behaviour at Merapi volcano (Java) revealed from an active seismic experiment, *Geophys. J. Int.*, *145*, 579–592.

Westerhaus, M., D. Rebscher, W. Welle, A. Pfaff, A. Körner, and I. G. M. A. Nandaka (1998), Deformation measurements at the flanks of Merapi volcano, in *Decade-Volcanoes Under Investigation, 1st Merapi-Galeras Workshop, Potsdam June 25, 1998*, edited by J. Zschau and M. Westerhaus, *Mitt. III/1998*, pp. 93–99, *Dtsch. Geophys. Ges.*, Potsdam, Germany.

G. Asch, M. Bohm, B.-G. Lühr, and A. Manzanares, GeoForschungs-Zentrum Potsdam, Telegrafenberg, D-14473 Potsdam, Germany.

K. S. Brotopuspito, Gadjah Mada University, Bulaksumur, Yogyakarta 55281, Indonesia.

P. Fauzi, Meteorological and Geophysical Agency, Jalan Angkasa 1 No. 2, Kemayoran, Jakarta, Pusat 10720, Indonesia.

H. Kopp, IFM-GEOMAR, FB4 Dynamics of the Oceanfloor, Wischhofstr 1-3, Kiel, D-24148, Germany.

I. Koulakov, Trofimuk Institute of Petroleum Geology and Geophysics SB RAS, Prospekt Koptyuga, 3, Novosibirsk, 630090, Russia. (kul@uiggm.nsc.ru)

M. A. Purbawinata, Directorate of Volcanology and Geological Hazard Mitigation, Jalan Diponegoro 57, Bandung 40122, Indonesia.

N. T. Puspito, Institut Teknologi Bandung, Jalan Tamansari, 64 Bandung 40116, Indonesia.

W. Rabbel, Applied Geophysics Section, Institute of Geosciences, Christian-Albrechts-Universität zu Kiel, Otto-Hahn Platz 1, D-24118 Kiel, Germany.

A. Ratdomopurbo, Volcanological Technology Research Center, Jalan Cendana 15, Yogyakarta 55166, Indonesia.

E. Shevkunova, Geophysical Survey SB RAS, 630090, Ac. Koptyug Pr., 3 Novosibirsk, Russia.